Accelerated Free-Breathing 5D Multi-Echo Respiratory Motion-Resolved R2*, PDFF, and QSM Using Novel Composite Total Variation

MungSoo Kang[1,2], Or Alus[1,2], and Youngwook Kee[1,2]*

[1] Stony Brook University, Stony Brook NY 11794, USA
[2] Memorial Sloan Kettering Cancer Center, New York NY 10065, USA
*Corresponding author (`youngwook.kee@stonybrook.edu`)

Abstract. We introduce a novel composite total variation (TV) and its solution algorithm with their application to multi-echo, respiratory motion-resolved 5D (3D space + 1D respiratory motion + 1D echo signal evolution) compressed sensing (CS) abdominal MR image reconstruction. The proposed formalism ensures a sparse representation between multi-echo images with varying contrast—a vital feature that needs to be preserved—making it highly suitable for applications in multi-dimensional computational/quantitative imaging. The key idea of the proposed composite TV and its formal definition were inspired by the observation that the spatial gradient of difference images in multi-echo MRI appears sparse. Throughout extensive experiments on a small number of healthy volunteers, we have demonstrated improved performance of the proposed method in 5D motion-resolved CS reconstruction of multi-echo MRI data compared to the state-of-the-art method. We have also demonstrated improved performance of the proposed method in quantitative tissue parameter mapping (such as R2*, proton density fat fraction, and quantitative susceptibility mapping) across a wide range of undersampling factors. In conclusion, the proposed method enables vastly accelerated motion-resolved multi-echo CS-MRI minimally impacting the quantification of downstream tissue parameters.

Keywords: Compressed sensing · Model-based MR image reconstruction · Non-Cartesian multi-echo MRI. · Quantitative imaging

1 Introduction

Free-breathing multi-echo gradient echo (mGRE) MRI has recently emerged as a new imaging technique [1,14,17,21,22]. This technique acquires 3D volumetric images at multiple time points, encoding a 1D echo signal evolution at each voxel over time (on the order of milliseconds). The slower, second-scale respiratory motion embedded in the 4D spatiotemporal mGRE data can then be retrospectively resolved to mitigate motion-induced errors [8]. Free-breathing mGRE MRI with respiratory motion-resolved reconstruction has enabled voxel-wise quantification of R2*, proton density fat fraction (PDFF), and tissue magnetic susceptibility [14, 21, 22], offering great potential for use in patient populations—such as children or certain adults—where maintaining a breath-hold is impractical.

Despite its free-running and/or free-breathing capability, a major challenge in its clinical adoption is the lengthy acquisition time. This increases the likelihood of subject bulk motion that may not be adequately corrected or resolved under the typical assumption of strictly periodic motion (e.g., respiration). Moreover, there is a trade-off between high isotropic resolution and maintaining a shorter acquisition time. Accurate tissue parameter mapping often requires high isotropic resolution to avoid undesirable bias [16, 26]. Ideally, such a 5D imaging dataset would require multi-way array or tensor-based reconstruction/processing, but this area has not been extensively explored. One approach is to reconstruct all echoes simultaneously using ℓ_1 coupling [14], which results in a 4D echo-by-echo reconstruction that neglects the correlations between echoes. We note that several MRI reconstruction studies have explored TV-like joint smoothness constraints across images with significant contrast differences [2, 10, 11, 23]. Related TV-based regularizers for multi-contrast images have also been proposed in the image processing literature [4, 5, 18, 25]. Finally, low-rank methods [3, 6, 24] have shown promise. These studies were primarily designed for 2D/3D Cartesian imaging of static organs like the brain with little attention to tissue parameter mapping and have not been extended to 5D non-Cartesian motion-resolved mGRE MRI.

We hypothesize that true 5D processing enables further acceleration by introducing a novel generalization of TV tailored for free-breathing mGRE data. The proposed reconstruction approach exploits data sparsity among the multi-echo images through this generalized TV—referred to as *composite TV* throughout the paper. Integrating composite TV along the echo dimension and temporal TV along the motion-state dimension, our method performs multi-way array (5D) reconstruction, substantially accelerating free-breathing mGRE MRI. Note that classical TV and existing generalizations do not account for the notion of sparsity among multi-echo images because the contrast differences between echoes are not inherently sparse and must be preserved. The challenge is thus to devise a new regularizer such that it preserves image contrast while sparsifying relevant features across echoes. Our contributions/findings are as follows: (a) We introduce a novel composite TV that imposes sparsity between echoes; (b) We derive a solution algorithm compactly expressed via the standard primal-dual hybrid gradient (PDHG) method; and (c) We demonstrate the feasibility of highly accelerated free-breathing, motion-resolved mGRE MRI for liver R2*, PDFF, and quantitative susceptibility mapping (QSM) with high isotropic resolution.

2 Theory

2.1 Problem Formulation & Prior Works

Let Q be the number of fully-sampled k-space samples that meet the Nyquist sampling criterion. Let T be the number of latent respiratory phases (from the end-expiratory to end-inspiratory states) embedded in the incoherently sampled k-space samples $g \in \mathbb{C}^Q$ during free breathing. Let $P_\pi : \mathbb{C}^Q \to \mathbb{C}^Q$ be some permutation matrix that reorders $g = (g^1, \ldots, g^Q)$ to $P_\pi g = \tilde{g} = (\tilde{g}^1, \ldots, \tilde{g}^Q)$ such that the $\tilde{g}^{(n-1)\lfloor Q/T \rfloor + 1}, \ldots, \tilde{g}^{n\lfloor Q/T \rfloor}$ belong to the n-th motion state where $n = 1, \ldots, T$. Notice that the k-space samples that fall into each motion state n is retrospectively undersampled by a factor of T, i.e., the number of k-space measurements for each motion state is approximately $\lfloor Q/T \rfloor$. As g is incoherently sampled uniformly covering the entire k-space (so is $\tilde{g}$), one can utilize CS reconstruction.

Let N be the image size, and let $u \in \mathbb{C}^{N \cdot T}$ be a set of vectorized motion-resolved images to be reconstructed from $\tilde{g}$. Feng et al. [8] cast the problem by incorporating the ℓ_1-norm of the forward difference between motion states into the cost function as follows:

$$\Psi_{\text{Feng}}(u; \tilde{g}) \triangleq ||Au - \tilde{g}||_W^2 + \lambda_m ||\Delta_m^+ u||_1, \tag{1}$$

where $A : \mathbb{C}^{N \cdot T} \to \mathbb{C}^Q$ is the MRI encoding operator, $\Delta_m^+ : \mathbb{C}^{N \cdot T} \to \mathbb{C}^{N \cdot T}$ is the forward difference operator along the motion state, and $\lambda_m > 0$. The weighted least-squares fidelity $||Au - \tilde{g}||_W^2$ is given as $(Au - \tilde{g})^{\mathsf{H}} W (Au - \tilde{g})$ where the density compensation factor is commonly chosen for W and A^{H} is the adjoint of A (the conjugate transpose $A^{\mathsf{H}} = \overline{A}^\top$).

Suppose that we are now given an mGRE k-space data $g_1, \ldots, g_E$ where $g_j \in \mathbb{C}^Q$ for $j = 1, \ldots, E$, and some permutation matrix P_π. Then, $\tilde{g}_j$ is a reordering of g_j by P_π, i.e., $\tilde{g}_j = P_\pi g_j$. Let $u_1, \ldots, u_E \in \mathbb{C}^{N \cdot T}$ be a set of motion-resolved mGRE images. Kang et al. [14] extended (1) as follows:

$$\Psi_{\text{Kang}}(u_1, \ldots, u_E; \tilde{g}_1, \ldots, \tilde{g}_E) \triangleq \sum_{j=1}^{E} ||Au_j - \tilde{g}_j||_W^2 + \lambda_m \sum_{j=1}^{E} ||\Delta_m^+ u_j||_1. \tag{2}$$

Note that an extension of (2) to multi-coil reconstruction is straightforward.

2.2 Proposed Method & Numerical Optimization

Denoting the concatenation of $u_1, \ldots, u_E$ as $\underline{u} \in \mathbb{C}^{N \cdot T \cdot E}$ and the concatenation of $\tilde{g}_1, \ldots, \tilde{g}_E$ as $\underline{\tilde{g}} \in \mathbb{C}^{Q \cdot E}$, we propose to minimize the following cost function

$$\Psi_{\text{Ours}}(\underline{u}; \underline{\tilde{g}}) \triangleq ||A\underline{u} - \underline{\tilde{g}}||_W^2 + \lambda_m ||\Delta_m^+ \underline{u}||_1 + \lambda_e ||(\nabla_{\mathbf{x}} \circ \Delta_e^+)\underline{u}||_{2,1} \tag{3}$$

where $\nabla_{\mathbf{x}} : \mathbb{C}^{N \cdot T \cdot E} \to \mathbb{C}^{(N \cdot T \cdot E) \times 3}$ is the spatial gradient operator and $||\cdot||_{2,1}$ is a matrix norm that maps $\underline{v} \in \mathbb{C}^{(N \cdot T \cdot E) \times 3}$ to $\sum_i \sqrt{\sum_j |\underline{v}_{i,j}|^2}$ for $i = 1, \ldots, N \cdot T \cdot E$ and $j = 1, 2, 3$. Extending the operator A and the diagonal matrix W to accommodate the dimensions of the vectorized $\underline{u}$ and $\underline{\tilde{g}}$ is straightforward, and $\lambda_e > 0$ is a regularization parameter. The composite operator inside the $\ell_{2,1}$ norm extracts a contrast-invariant sparse representation—while contrast changes across echoes are not sparse, image edges remain largely sparse. Noise-like undersampling artifacts (as the difference of two Gaussians is also Gaussian), extracted with sparse

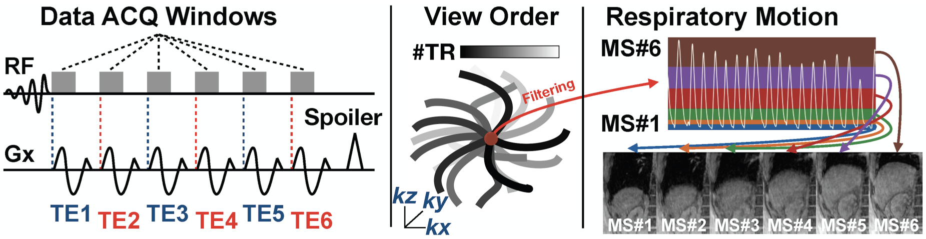

Fig. 1. Illustration of data acquisition and respiratory motion-resolved image reconstruction. Six echoes (TE1 to TE6) are sequentially acquired within a single TR as schematized in the pulse timing diagram. Cones readouts are uniformly distributed in k-space using a pseudorandom view order. The center of k-space (DC) is used to estimate the underlying respiratory motion. The number of motion states to be resolved is set to 6, and the corresponding respiratory motion-resolved images are shown.

edges, are selectively suppressed by the $\ell_{2,1}$ norm, effectively preserving sharp edges.

We provide implementation details of a numerical method that solves the cost function (3) in a multi-coil setting. Let C be the number of coil elements; and let $I_\otimes : \mathbb{C}^{N \cdot T \cdot E} \to \mathbb{C}^{(C+3) \cdot N \cdot T \cdot E}$ be a linear operator such that $\underline{u} \mapsto I_\otimes \underline{u} = [\underbrace{\underline{u}^\top, \dots, \underline{u}^\top}_{C\,\text{times}}, \underline{u}^\top, \underline{u}^\top, \underline{u}^\top]^\top$. Then, the minimization problem (3) can be reformulated as the following saddle-point problem [7]:

$$\text{Find } \underline{u}, v \text{ such that } \min_{\underline{u}} \max_{v} \operatorname{Re} \langle (K \circ I_\otimes) \underline{u}, v \rangle - H v, \tag{4}$$

where the linear operator $K : \mathbb{C}^{(C+3) \cdot N \cdot T \cdot E} \to \underbrace{\mathbb{C}^{Q \cdot E} \times \cdots \times \mathbb{C}^{Q \cdot E}}_{C\,\text{times}} \times \mathbb{C}^{N \cdot T \cdot E} \times \mathbb{C}^{(N \cdot T \cdot E) \times 3}$ is defined as

$$K = \begin{bmatrix} W^{1/2} F S_1 & \cdots & 0 & 0 & 0 \\ \vdots & \ddots & \vdots & \vdots & \vdots \\ 0 & \cdots & W^{1/2} F S_C & 0 & 0 \\ 0 & \cdots & 0 & \Delta_m^+ & 0 \\ 0 & \cdots & 0 & 0 & \nabla_{\mathbf{x}} \circ \Delta_e^+ \end{bmatrix}; \tag{5}$$

where F is the nonuniform Fourier transform operator, $S_1, \dots, S_C$ are coil sensitivity maps, and $H : \underbrace{\mathbb{C}^{Q \cdot E} \times \cdots \times \mathbb{C}^{Q \cdot E}}_{C\,\text{times}} \times \mathbb{C}^{N \cdot T \cdot E} \times \mathbb{C}^{(N \cdot T \cdot E) \times 3} \to \overline{\mathbb{R}}$, $v := (p_1, \dots, p_C, q_m, q_{\mathbf{x}}) \mapsto H(p_1, \dots, p_C, q_m, q_{\mathbf{x}}) = \sum_{c=1}^{C} \operatorname{Re} \langle W^{1/2} \tilde{g}_c, p_c \rangle + (1/2) ||p_c||_2^2 + \delta_{Q_m}(q_m) + \delta_{Q_{\mathbf{x}}}(q_{\mathbf{x}})$. Here, $\delta_{Q_m}(q_m) = 0$ if $q_m \in Q_m$ and $+\infty$ elsewhere; $\delta_{Q_{\mathbf{x}}}(\cdot)$ is similarly defined.

The convex sets Q_m and $Q_{\mathbf{x}}$ are given as $Q_m = \{q_m \in \mathbb{C}^{N \cdot T \cdot E} : ||q_m||_\infty \leq \lambda_m\}$ and $Q_{\mathbf{x}} = \{q_{\mathbf{x}} \in \mathbb{C}^{(N \cdot T \cdot E) \times 3} : ||q_{\mathbf{x}}||_\infty \leq \lambda_e\}$, respectively. Then, a saddle

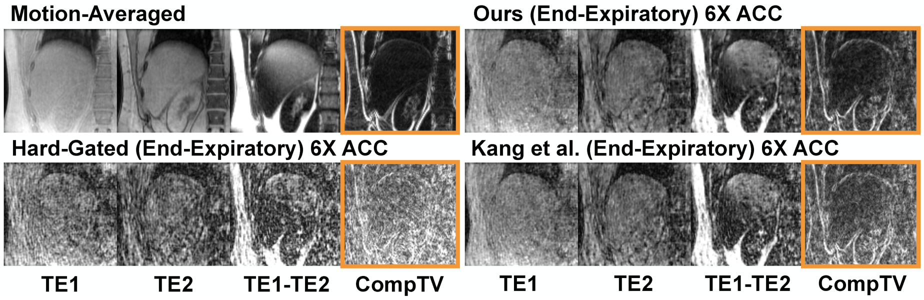

Fig. 2. Desired effect of incorporating $||\nabla_{\mathbf{x}} \circ \Delta_e^+ \cdot ||_{2,1}$; see Section 4.

point $(\underline{u}, v)$ that satisfies $0 \in I_{\otimes}^H(K^H \hat{v})$ and $\partial H(\hat{v}) \in K(I_{\otimes}\hat{\underline{u}})$ can be found by the primal-dual hybrid gradient (PDHG) method [7] as follows.

$$v^{k+1} = (I + \sigma \partial H)^{-1}(v^k + \sigma K I_{\otimes} \tilde{\underline{u}}^k); \tag{6a}$$

$$\underline{u}^{k+1} = \underline{u}^k - \tau I_{\otimes}^H K^H v^{k+1}; \tag{6b}$$

$$\tilde{\underline{u}}^{k+1} = 2\underline{u}^{k+1} - \underline{u}^k. \tag{6c}$$

The resolvent (proximal) operator $(I + \sigma\partial H)^{-1}$ associated with $\mathrm{Re}\,\langle W^{1/2}\tilde{g}_c, p_c\rangle + (1/2)||p_c||_2^2$w can be derived as

$$\hat{r}_c = \underset{r_c}{\mathrm{argmin}}\, \frac{||r_c - p_c||_2^2}{2\sigma} + \mathrm{Re}\,\langle W^{1/2}\tilde{g}_c, r_c\rangle + \frac{1}{2}||r_c||_2^2 \iff \hat{r}_c = \frac{p_c - \sigma W^{1/2}\tilde{g}_c}{1+\sigma},$$

for $c = 1, \ldots, C$. The derivation of the projection operators associated with the indicator functions $\delta_{Q_m}(\cdot)$ and $\delta_{Q_{\mathbf{x}}}(\cdot)$ is straightforward using the Moreau decomposition [20] and the soft-thresholding operator.

3 Experimental Methods

MRI Data Acquisition & Imaging Parameters. Upon IRB approval, 3D mGRE cones MRI implemented based on [9,14,17] was performed on 3 healthy subjects using a 3T clinical scanner (GE Healthcare, Waukesha, WI). All subjects underwent the imaging procedure with free breathing and one of the subjects was instructed to perform deep breathing throughout the scan. Imaging parameters for the 3D mGRE cones MRI were: initial TE/ΔTE/TR = 0.032/1.4-1.5/11.4-11.5 ms, #TEs = 6 (#shots = 1, ETL = 6), FA = 3°, in-plane resolution = 2×2 mm^2, slice thickness = 2 mm, rBW = 1106-1315 Hz/Px, scan time = 5 min 15 sec to 7 min 37 sec (without acceleration), readout duration = ∼1 ms, and #interleaves = 27,651 to 39,699. Echo spacing for cone acquisition was set at 1.4-1.5 ms to facilitate in- and out-of-phase data acquisition. This was combined with an ultrashort initial TE to capture the rapid T2* signal decay. The data acquisition scheme and reconstruction strategy are illustrated in Fig. 1.

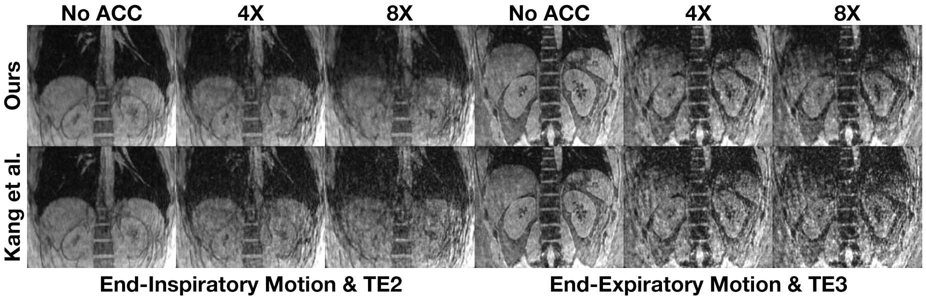

Fig. 3. Reconstructed images of a healthy subject instructed to perform deep breathing with *effective* undersampling factors 6X (i.e., no ACC and 6 motion states), 24X (i.e., 4X ACC and 6 motion states), and 48X (i.e., 8X ACC and 6 motion states) are shown.

Image Reconstruction & Tissue Parameter Mapping. In our context, *acceleration* (ACC) refers to retrospective undersampling applied prior to motion binning, with the goal of reducing scan time. The fully-sampled k-space raw data was retrospectively undersampled by factors ranging from 2X to 10X, achieved by discarding the corresponding number of readouts. This was done in a manner that allows for straightforward implementation of prospective undersampling. Then, *motion binning* which is another form of retrospective undersampling was carried out subsequent to 2X to 10X ACC. In our paper, the number of motion states was set to 6; therefore, the overall *effective* undersampling factors were from 6X (No ACC) to 60X (10X ACC with 6 motion states).

Implemented reconstruction methods were: 1) motion-averaged gridding, 2) hard-gated gridding applied to each motion state, 3) motion-resolved (2), and 4) the proposed (3) reconstructions. For 2), 3), and 4), the center of k-space of each cones readout was extracted to estimate the respiratory motion [12,13] as illustrated in Fig. 1. For 3) and 4), the PDHG algorithm described in Section 2.2 was implemented in Python using the nuFFT routine in SigPy [19]. All reconstructions were run on a 4-way Nvidia A100 GPU machine (80GB of video memory per GPU). These GPUs were utilized concurrently. We considered the following combinations of regularization parameters: $10^{-7} \leq \lambda_m \leq 10^{-4}$ and $10^{-7} \leq \lambda_e \leq 10^{-4}$ for all *effective* undersampling factors = {6X, 12X, 24X, 36X, 48X, 60X} per subject. From our subjective evaluation, we sequentially chose the best $\lambda_m = 7 \times 10^{-6}$ and $\lambda_e = 1 \times 10^{-6}$ for all subjects. Using the standard post-processing pipeline [14,17], R2*, PDFF, and QSM were generated from the reconstructed complex-valued mGRE images. The model $s(\mathbf{x},t) = (\rho_w(\mathbf{x}) + \rho_f(\mathbf{x})e^{-i2\pi f_{cs}t})e^{-R2^*(\mathbf{x})t - i2\pi f_b(\mathbf{x})t}$ for $t = \mathrm{TE}_1, \ldots, \mathrm{TE}_6$ was fitted to the reconstructed mGRE images with respect to ρ_w (water), ρ_f (fat), $R2^*$, and f_b (B0 field) voxel by voxel, i.e., for all $\mathbf{x}$. Then, PDFF was computed as $|\rho_f(\mathbf{x})|/(|\rho_w(\mathbf{x})| + |\rho_w(\mathbf{x})|)$. For QSM, the fat-referenced nonlinear dipole inversion was performed with the same set of reconstruction parameters and background field removal presented in [14].

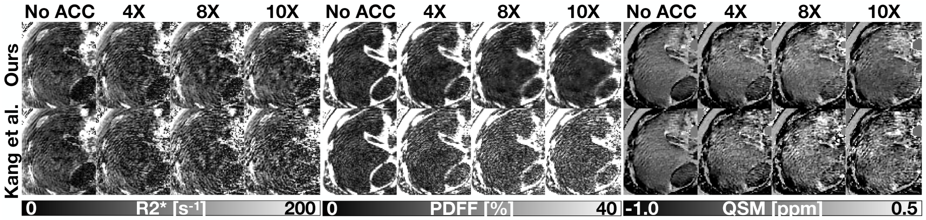

Fig. 4. Quantitative parameter maps of a healthy subject with *effective* undersampling factors 6X (i.e., no ACC and 6 motion states), 24X (4X ACC and 6 motion states), 48X (8X ACC and 6 motion states), and 60X (10X ACC and 6 motion states) are shown.

Image Quality Assessment & ROI-based Quantification. Due to the nature of the study, acquiring fully sampled motion-resolved MRI data is infeasible as subjects breathe freely during the 6-8 minute imaging period. The concept of "ground truth" is not applicable in this context; therefore, we used the motion-resolved reconstruction (2), i.e., [14] from 6X undersampled k-space data (no ACC and 6 motion states) was considered as the reference to calculate the relative error, PSNR, SSIM, and MSE. To assess contrast fidelity, a region of interest (ROI) with a radius of 10 voxels was placed in the tissue of interest (liver parenchyma) on three consecutive slices of the computed tissue parameter maps (R2*, PDFF, and QSM), while avoiding large vessels. Then, mean ± SD was calculated for 6–60X undersampling factors and compared between the methods.

4 Experimental Results

The desired effect of incorporating $||\nabla_{\mathbf{x}} \circ \Delta_e^+ \cdot ||_{2,1}$ is demonstrated in Fig. 2. The key observation is that the motion-averaged mGRE images (neither accelerated nor retrospectively undersampled for motion binning) exhibit a sparse representation after the $\nabla \circ \Delta_e^+$ operation (image in orange bounding box). The operator Δ_e^+ alone does not provide such a desired representation (third column from the left) due to the difference in contrast between TE1 and TE2 images, which encodes important tissue information. Hard-gated reconstruction of the same subject (6X ACC and 6 motion states, i.e., overall 36X undersampling), exhibits a noisy representation after the $\nabla \circ \Delta_e^+$ operation. This noisy representation is due to undersampling artifacts across the echoes. Compared to Kang et al. [14] (6X ACC and 6 motion states), the proposed method (6X ACC and 6 motion states) produces a less noisy representation after the $\nabla \circ \Delta_e^+$ operation, as a result of reduced undersampling artifacts.

Reconstructed images of a healthy volunteer instructed to perform deep breathing are shown in Fig. 3 with different undersampling factors. Compared to Kang et al. [14] where image quality rapidly deteriorates due to increased undersampling artifacts, the proposed method demonstrates the ability to maintain visual image quality. The relative differences between the reference (Kang et al.

Table 1. Image quality assessment and ROI-based measurements. PSNR/SSIM (higher the better); MSE (lower the better). R2*/PDFF/QSM are reported as mean ± SD.

Subj #1	Metric	No ACC	2X	4X	6X	8X	10X
Ours	PSNR	53.9393	35.2265	32.8812	32.0261	30.7820	29.0965
	SSIM	0.9951	0.9003	0.8265	0.8021	0.7577	0.7596
	MSE	0.0040	0.3002	0.5151	0.6272	0.8352	1.2313
[14]	PSNR	Inf	35.0066	32.1682	31.1111	29.6637	28.4149
	SSIM	1	0.8946	0.7850	0.7389	0.6738	0.6856
	MSE	0	0.3157	0.6070	0.7743	1.0805	1.4405

Subj #1	Metric	No ACC	4X	8X	10X
Ours	R2*	44.01±24.87	55.00±28.20	63.80±33.81	72.51±37.31
	PDFF	6.79±3.00	5.61±3.06	6.91±3.15	5.71±2.96
	QSM	−0.19±0.09	−0.21±0.13	−0.25±0.18	−0.28±0.17
[14]	R2*	44.01±25.55	53.26±30.83	64.95±41.61	72.24±46.38
	PDFF	7.32±3.45	8.59±4.46	10.69±6.14	10.89±5.54
	QSM	−0.19±0.10	−0.18±0.17	−0.33±0.27	−0.33±0.25

Subj #2	Metric	No ACC	2X	4X	6X	8X	10X
Ours	PSNR	55.3231	39.2684	37.3378	35.8115	34.8276	34.2043
	SSIM	0.9936	0.9347	0.9055	0.8798	0.8551	0.8477
	MSE	0.0029	0.1183	0.1846	0.2623	0.3290	0.3798
[14]	PSNR	Inf	38.7403	36.3399	34.5567	33.3129	32.7903
	SSIM	1	0.9201	0.8611	0.8086	0.7581	0.7418
	MSE	0	0.1337	0.2323	0.3502	0.4663	0.5260

Subj #2	Metric	No ACC	4X	8X	10X
Ours	R2*	34.00±19.52	33.69±23.86	43.02±23.79	47.67±24.62
	PDFF	7.85±3.39	7.98±3.64	7.58±2.97	8.68±3.10
	QSM	−0.41±0.10	−0.32±0.16	−0.27±0.14	−0.43±0.13
[14]	R2*	34.38±20.78	37.33±27.67	49.83±33.67	56.97±37.34
	PDFF	8.75±4.12	11.29±5.69	12.88±6.41	14.14±7.41
	QSM	−0.38±0.12	−0.28±0.22	−0.20±0.26	−0.23±0.30

Subj #3	Metric	No ACC	2X	4X	6X	8X	10X
Ours	PSNR	54.0232	39.3264	36.4982	35.1042	34.6145	33.6208
	SSIM	0.9899	0.9399	0.8999	0.8738	0.8626	0.8440
	MSE	0.0040	0.1168	0.2240	0.3087	0.3456	0.4344
[14]	PSNR	Inf	38.6929	35.6087	33.9137	33.2628	32.2565
	SSIM	1	0.9200	0.8450	0.7804	0.7440	0.7035
	MSE	0	0.1351	0.2749	0.4061	0.4718	0.5948

Subj #3	Metric	No ACC	4X	8X	10X
Ours	R2*	65.38±24.39	90.28±37.10	122.03±56.39	162.09±67.02
	PDFF	8.69±2.67	9.37±3.36	10.89±4.06	12.16±4.88
	QSM	−0.30±0.07	−0.32±0.12	−0.11±0.20	−0.27±0.85
[14]	R2*	65.27±25.28	89.98±43.13	116.61±65.33	150.41±85.18
	PDFF	9.10±3.42	11.47±5.05	15.50±6.91	17.54±8.11
	QSM	−0.32±0.08	−0.35±0.16	−0.49±0.32	0.02±1.06

with no ACC) and the proposed method (vs Kang et al.) were 28% (vs 31%), 39% (vs 45%), 46% (vs 55%), 49% (vs 60%), and 54% (vs 67%) for 2X to 10X, confirming the difference in visual image quality. For the other two subjects, the relative differences were: 23% (vs 24%), 32% (vs 35%), 35% (vs 40%), 41% (vs 47%), and 44% (vs 50%) for 2X to 10X (Subj #1); and 25% (vs 27%), 32% (vs 36%), 37% (vs 44%), 42% (vs 51%), and 44% (vs 54%) for 2X to 10X (Subj #2). Furthermore, consistently improved PSNR, SSIM, and MSE in Table 1 agree with the above observations and relative differences. R2*, PDFF, and QSM of a healthy subject with acceleration factors ranging from no ACC to 10X are shown in Fig. 4. Unlike Kang et al. [14] where image quality notably deteriorates, which may be characterized by "salt and pepper" noise, the proposed method shows minimally affected image quality. ROI-based R2*, PDFF, and QSM measurements of healthy volunteers are presented in Table 1. The proposed method exhibits smaller standard deviations across all undersampling factors than Kang et al. [14], suggesting a higher precision level. The visual assessment of Fig. 4 can be confirmed by standard deviations of the measurement.

5 Discussion and Conclusion

Although the feasibility of the proposed method was only demonstrated on a small number of subjects, the proposed novel composite TV and its solution algorithm has enabled 5D CS reconstruction of non-Cartesian mGRE MRI data across a wide range of *effective* undersampling factors, from 6X to 60X. Future work will include a larger patient cohort, particularly those with known iron overload or steatosis to further strengthen the study. In addition, the proposed method will be applied to prospectively undersampled k-space data to validate its robustness in providing reliable liver tissue parameters, comparing with our recent study that demonstrated the feasibility of 5D reconstruction by exploiting sparsity across spatial, motion, and echo dimensions [15].

Acknowledgement. This work was supported in part by National Institutes of Health under Award Numbers: R21EB033985 and R21DK137146.

Disclosure of Interests. The authors have no competing interests to declare that are relevant to the content of this article.

References

1. Armstrong, T., Dregely, I., Stemmer, A., Han, F., Natsuaki, Y., Sung, K., Wu, H.H.: Free-breathing liver fat quantification using a multiecho 3d stack-of-radial technique. Magnetic resonance in medicine **79**(1), 370–382 (2018)
2. Bilgic, B., Goyal, V.K., Adalsteinsson, E.: Multi-contrast reconstruction with bayesian compressed sensing. Magnetic resonance in medicine **66**(6), 1601–1615 (2011)

3. Bilgic, B., Kim, T.H., Liao, C., Manhard, M.K., Wald, L.L., Haldar, J.P., Setsompop, K.: Improving parallel imaging by jointly reconstructing multi-contrast data. Magnetic resonance in medicine **80**(2), 619–632 (2018)
4. Blomgren, P., Chan, T.F.: Color tv: total variation methods for restoration of vector-valued images. IEEE transactions on image processing **7**(3), 304–309 (1998)
5. Bresson, X., Chan, T.F., et al.: Fast dual minimization of the vectorial total variation norm and applications to color image processing. Inverse problems and imaging **2**(4), 455–484 (2008)
6. Bustin, A., Lima da Cruz, G., Jaubert, O., Lopez, K., Botnar, R.M., Prieto, C.: High-dimensionality undersampled patch-based reconstruction (hd-prost) for accelerated multi-contrast mri. Magnetic resonance in medicine **81**(6), 3705–3719 (2019)
7. Chambolle, A., Pock, T.: A first-order primal-dual algorithm for convex problems with applications to imaging. Journal of mathematical imaging and vision **40**, 120–145 (2011)
8. Feng, L., Axel, L., Chandarana, H., Block, K.T., Sodickson, D.K., Otazo, R.: Xd-grasp: golden-angle radial mri with reconstruction of extra motion-state dimensions using compressed sensing. Magnetic resonance in medicine **75**(2), 775–788 (2016)
9. Gurney, P.T., Hargreaves, B.A., Nishimura, D.G.: Design and analysis of a practical 3d cones trajectory. Magnetic Resonance in Medicine: An Official Journal of the International Society for Magnetic Resonance in Medicine **55**(3), 575–582 (2006)
10. Haldar, J.P., Liang, Z.P.: Joint reconstruction of noisy high-resolution mr image sequences. In: 2008 5th IEEE International Symposium on Biomedical Imaging: from Nano to Macro. pp. 752–755. IEEE (2008)
11. Haldar, J.P., Wedeen, V.J., Nezamzadeh, M., Dai, G., Weiner, M.W., Schuff, N., Liang, Z.P.: Improved diffusion imaging through snr-enhancing joint reconstruction. Magnetic resonance in medicine **69**(1), 277–289 (2013)
12. Jiang, W., Ong, F., Johnson, K.M., Nagle, S.K., Hope, T.A., Lustig, M., Larson, P.E.: Motion robust high resolution 3d free-breathing pulmonary mri using dynamic 3d image self-navigator. Magnetic resonance in medicine **79**(6), 2954–2967 (2018)
13. Kang, M., Wen, Y., Carl, M., Behr, G., Otazo, R., Kee, Y.: Free-breathing r2* mapping for hepatic iron quantification using respiratory motion-resolved 3d multi-echo ute cones mri. In: Proceedings of the 2022 ISMRM & ISMRT Annual Meeting, London, England, UK (Abstract# 1338)
14. Kang, M., Behr, G.G., Jafari, R., Gambarin, M., Otazo, R., Kee, Y.: Free-breathing high isotropic resolution quantitative susceptibility mapping (qsm) of liver using 3d multi-echo ute cones acquisition and respiratory motion-resolved image reconstruction. Magnetic Resonance in Medicine (2023)
15. Kang, M., Otazo, R., Behr, G., Kee, Y.: 5d image reconstruction exploiting space-motion-echo sparsity for accelerated free-breathing quantitative liver mri. Medical Image Analysis **102**, 103532 (2025)
16. Karsa, A., Punwani, S., Shmueli, K.: The effect of low resolution and coverage on the accuracy of susceptibility mapping. Magnetic resonance in medicine **81**(3), 1833–1848 (2019)
17. Kee, Y., Sandino, C.M., Syed, A.B., Cheng, J.Y., Shimakawa, A., Colgan, T.J., Hernando, D., Vasanawala, S.S.: Free-breathing mapping of hepatic iron overload in children using 3d multi-echo ute cones mri. Magnetic Resonance in Medicine **85**(5), 2608–2621 (2021)

18. Molina, R., Mateos, J., Katsaggelos, A.K., Vega, M.: Bayesian multichannel image restoration using compound gauss-markov random fields. IEEE Transactions on Image Processing **12**(12), 1642–1654 (2003)
19. Ong, F., Lustig, M.: Sigpy: a python package for high performance iterative reconstruction. In: Proceedings of the ISMRM 27th Annual Meeting, Montreal, Quebec, Canada. vol. 4819 (2019)
20. Parikh, N., Boyd, S., et al.: Proximal algorithms. Foundations and trends® in Optimization **1**(3), 127–239 (2014)
21. Schneider, M., Benkert, T., Solomon, E., Nickel, D., Fenchel, M., Kiefer, B., Maier, A., Chandarana, H., Block, K.T.: Free-breathing fat and r2* quantification in the liver using a stack-of-stars multi-echo acquisition with respiratory-resolved model-based reconstruction. Magnetic resonance in medicine **84**(5), 2592–2605 (2020)
22. Tan, Z., Unterberg-Buchwald, C., Blumenthal, M., Scholand, N., Schaten, P., Holme, C., Wang, X., Raddatz, D., Uecker, M.: Free-breathing liver fat, r2* and b0 field mapping using multi-echo radial flash and regularized model-based reconstruction. IEEE Transactions on Medical Imaging (2022)
23. Trzasko, J., Manduca, A.: Group sparse reconstruction of vector-valued images. In: Proc Int Soc Magn Reson Med. vol. 19, p. 2839 (2011)
24. Trzasko, J.D.: Exploiting local low-rank structure in higher-dimensional mri applications. In: Wavelets and Sparsity XV. vol. 8858, pp. 551–558. SPIE (2013)
25. Yang, J., Yin, W., Zhang, Y., Wang, Y.: A fast algorithm for edge-preserving variational multichannel image restoration. SIAM Journal on Imaging Sciences **2**(2), 569–592 (2009)
26. Zhou, D., Cho, J., Zhang, J., Spincemaille, P., Wang, Y.: Susceptibility underestimation in a high-susceptibility phantom: dependence on imaging resolution, magnitude contrast, and other parameters. Magnetic resonance in medicine **78**(3), 1080–1086 (2017)